# Copper Ferrite–Graphene Hybrid: A Multifunctional Heteroarchitecture for Photocatalysis and Energy Storage

**7 AUTHORS**, INCLUDING:

**Qun Chen**
Central South University
**178** PUBLICATIONS **1,321** CITATIONS

SEE PROFILE

**Hui Xia**
Nanjing University of Science and Technology
**91** PUBLICATIONS **2,358** CITATIONS

SEE PROFILE

**Xin Wang**
Nanjing University of Science and Technology
**951** PUBLICATIONS **11,503** CITATIONS

SEE PROFILE

# Copper Ferrite-Graphene Hybrid: A Multifunctional Heteroarchitecture for Photocatalysis and Energy Storage

Yongsheng Fu,[†,‡] Qun Chen,[‡] Mingyang He,[‡] Yunhai Wan,[§] Xiaoqiang Sun,*[,‡] Hui Xia,*[,§] and Xin Wang*[,†]

[†]Key Laboratory for Soft Chemistry and Functional Materials, Nanjing University of Science and Technology, Ministry of Education, Nanjing 210094, China

[‡]Key Laboratory of Fine Petrochemical Engineering, Changzhou University, Changzhou 213164, China

[§]School of Materials Science and Engineering, Nanjing University of Science and Technology, Nanjing 210094, China

**S** *Supporting Information*

**ABSTRACT:** A straightforward strategy is designed for the fabrication of $CuFe_2O_4$-graphene heteroarchitecture via a one-step hydrothermal route to allow multifunctional properties, i.e., magnetic cycling, high photocatalytic activity under visible light irradiation, and excellent electrochemical behaviors for use as the anode in lithium-ion batteries (LIBs). Transmission electron microscopy (TEM) observations indicate that graphene sheets are exfoliated and decorated with hexagonal $CuFe_2O_4$ nanoflakes. The photocatalytic activity measurements demonstrate that the combination of $CuFe_2O_4$ and graphene results in a dramatic conversion of the inert $CuFe_2O_4$ into a highly active catalyst for the degradation of methylene blue (MB) under visible light irradiation. $CuFe_2O_4$ nanoparticles themselves have excellent magnetic properties, which makes the $CuFe_2O_4$-graphene heteroarchitecture magnetically recyclable in a suspension system. It should be pointed out that the $CuFe_2O_4$-graphene (with 25 wt % graphene) heteroarchitecture as anode material for LIBs shows a high specific reversible capacity up to 1165 mAh g$^{-1}$ with good cycling stability and rate capability. The superior photocatalytic activity and electrochemical performance of the $CuFe_2O_4$-graphene nanocomposite can be attributed to its unique heteroarchitechture, which provides the remarkable synergistic effect between the $CuFe_2O_4$ nanoflakes and the graphene sheets.

## 1. INTRODUCTION

World energy use has increased sharply over the past several decades. Much of the growth in world energy consumption has been concentrated on the use of nonrenewable fossil fuels. The development of novel energy systems based on renewable energy sources is necessary to meet the ever-increasing demand for energy and to address environmental concerns.

In recent years, semiconductor photocatalysis, as a "green" technology, has been widely used for the treatment of polluted water created largely by the industrialized societies.[1−3] There have been many reports that various organic pollutants can be degraded completely through photocatalysis using metal oxide semiconductors or their heteroarchitectures under ultraviolet (UV) light irradiation.[4,5] However, it is well-known that, although the sun can provide an abundant source of photons, UV light accounts for only a small fraction (5%) of the solar energy compared with visible light (45%). Therefore, developing high-performance visible-light driven photocatalysts for environmental remediation has become one of the most active research topics in photocatalysis.[6−12]

Usually, photodegradation reactions are carried out in heterogeneous systems. The ability to reuse the suspended ultrafine photocatalysts after degradation can result in substantial cost savings. The introduction of magnetic nanoparticles to a variety of solid matrixes allows the combination of well-known procedures for photocatalyst heterogenization with techniques for magnetic separation.[13]

As an important class of magnetic materials, the spinel structured ferrites with general formula $MFe_2O_4$ (M is transition metal, such as Mn, Fe, Co, Ni, Cu, etc.) have been used in many applications. The properties of the ferrite can be varied by changing the identity of the divalent $M^{2+}$ cation. Among the ferrites, owing to unique electronic configuration of valence shell ($3d^{10}4s^1$), low price, environmental benignity, and the large abundance of Cu, $CuFe_2O_4$ has received great attention and is widely used in sensors, electronics, and catalysts in recent years.[14−16] Although $CuFe_2O_4$ alone is photocatalytically inactive under visible light irradiation, it is possible to improve the efficiency of the photoinduced charge separation in $CuFe_2O_4$ by coupling it with another semiconductor, resulting in enhanced photocatalytic performance. On the other hand, lithium-ion batteries (LIBs) have become a leading energy source for mobile electronic devices and it has been reported that the energy density of LIBs can be increased using the spinel ferrites as anode materials for LIBs.[17−20] For example, $CuFe_2O_4$ has been considered a promising anode material candidate for high-performance LIBs due to its high theoretical capacity (895 mAh g$^{-1}$).[20−22] However, it has also been found that the pure $CuFe_2O_4$ electrodes, suffering from low intrinsic electronic conductivity and huge volume change

during charge/discharge processes, showed low specific capacity and poor cycling stability, which impedes its effective use in LIBs. In recent years, various strategies have been employed to modify metal oxides to improve their electrochemical performance as anode materials in LIBs. One of the effective approaches is attaching transition metal oxide nanoparticles to carbon substrates. Theoretically, metal oxide/carbon hybrids are expected to be advanced electrode materials for LIBs, as a result of the combination of the electrochemical functionality of metal oxides and the electrical conductivity of carbon.[20]

As a rapidly rising star on the horizon of materials science, graphene has already revealed its use in many potential applications.[23−29] Because of its large specific surface area, remarkable electrical conductivity, excellent adsorptivity, ultrathin thickness, superior structural flexibility, and high chemical and thermal stability, graphene has been receiving recent attention as a support for catalysts and advanced anode material of LIBs.[30−36] Some efforts have been invested to utilize UV irradiation with graphene-metal oxide composites.[37−42] Attention has also been paid to graphene-based visible-light-driven photocatalysts.[43,44] Recently, we have introduced spinel structured ferrites ($MFe_2O_4$, M=Zn, Co, Ni, Mn) with graphene as magnetic visible-light driven catalyst.[45−48]

It is of great interest to explore a novel approach for imparting multifunctional properties onto graphene-ferrite heteroarchitectures. If that can be accomplished, then it may be possible to obtain widely useful hybrids with high specific reversible capacity, good cycling stability, and high rate capability for LIBs (as anode materials), which also have high performance under visible light irradiation as well as with great magnetic recycling property (as photocatalysts). Herein, we report the synthesis of a copper ferrite-graphene heteroarchitecture by a facile hydrothermal route to allow multifunctional properties to be imparted into such a structure. Interestingly, when combined with graphene, the inactive $CuFe_2O_4$ nanocrystals have been dramatically converted into a highly active catalyst with magnetic recycling properties for the degradation of methylene blue (MB) under visible light irradiation. Furthermore, the $CuFe_2O_4$-graphene (with 25 wt % graphene) heteroarchitecture exhibits superior battery performance with a high reversible capacity (1165 mAh g$^{-1}$), excellent cycling stability, and good rate capability compared with pure $CuFe_2O_4$. For the first time, we demonstrate that the graphene-$CuFe_2O_4$ nanocomposite could be a promising bifunctional material for both photocatalysis and energy storage.

## 2. EXPERIMENTAL SECTION

**2.1. Synthesis of CuFe$_2$O$_4$-Graphene Heteroarchitecture.** Graphite oxide (GO) was synthesized from purified natural graphite (Qingdao Zhongtian Company) with a mean particle size of 44 $\mu$m according to the method reported by Hummers and Offeman.[49] $CuFe_2O_4$-graphene heteroarchitectures with differing graphene content (10, 25, 30, 40 wt %) were synthesized by a hydrothermal method. A typical experiment procedure for the synthesis of $CuFe_2O_4$-graphene heteroarchitecture with 25 wt % graphene content is as follows: 160 mg of GO was dispersed into 120 mL of ethanol with sonication for 1 h. Then, 0.4832 g of $Cu(NO_3)_2 \cdot 3H_2O$ and 1.616 g of $Fe(NO_3)_3 \cdot 9H_2O$ were added to 30 mL of ethanol with stirring for 30 min at room temperature. The above two solutions were then mixed together and stirred for 30 min.

After that, the mixture was adjusted to a pH of 10.0 with 6 M NaOH solution and stirred for 30 min, yielding a stable bottle-green homogeneous emulsion. The resulting mixture was transferred into a 200 mL Teflon-lined stainless steel autoclave and heated to 180 °C for 24 h under autogenous pressure. The reaction mixture was allowed to cool to room temperature, and the precipitate was filtered, washed with distilled water five times, and dried in a vacuum oven at 60 °C for 12 h. The product was labeled as $CuFe_2O_4$-G(0.25). For comparison, the same method was used to synthesize pure $CuFe_2O_4$ without adding GO.

**2.2. Characterization.** The samples were characterized by X-ray photoelectron spectroscopy (XPS) using a RBD upgraded PHI-5000C ESCA system (Perkin-Elmer) with Mg K$\alpha$ radiation (h$\nu$=1253.6 eV). Raman spectra of the samples were acquired using a Renishaw inVia Reflex Raman Microprobe. Powder X-ray diffraction (XRD) patterns of the samples were obtained using a Bruker D8 Advanced diffractometer with Cu K$\alpha$ radiation. Morphological and structural characterizations of the samples were carried out by transmission electron microscopy (TEM, JEOL JEM2100) and field-emission scanning electron microscopy (FESEM, LEO1550). Nitrogen adsorption−desorption isotherms of the samples were measured at 77 K by a Micromeritics Model TriStar II 3020 volumetric analyzer. The magnetic properties of the nanocomposites were investigated by a vibrating sample magnetometer (VSM, HH-15).

Electrochemical impedance spectroscopy (EIS) measurements were performed using a CHI660B workstation. The test electrodes were prepared according to ref 50. EIS measurements were carried out in 1 M $H_2SO_4$ using a three-electrode cell system, with a platinum foil electrode as the counter electrode and a saturated calomel electrode (SCE) as the reference electrode. EIS measurements were performed with an AC voltage amplitude of 5 mV in a frequency range between 1 MHz and 5 mHz at an electrode potential of 0.5 V.

**2.3. Photocatalytic Activity Measurement.** The photocatalytic activity of the prepared samples was assessed by the degradation of MB under visible light irradiation. Photoirradiation was carried out using a 500 W xenon lamp through UV cutoff filters (JB450) to completely remove any radiation below 420 nm and to ensure illumination by visible-light only. The experiments were performed at 25 °C in the following manner: 0.025 g of photocatalyst was added to 100 mL of a 20 mg/L dye aqueous solution. Before starting the illumination, the reaction mixture was stirred for 60 min in the dark in order to reach the adsorption−desorption equilibrium between the dye and the catalyst. At a given time interval of irradiation, 5 mL aliquots were withdrawn, and then magnetically separated to remove essentially all the catalyst. The concentrations of the remnant dye were spectrophotometrically monitored by measuring the absorbance of solutions at 664 nm during the photodegradation process. Photocurrent was measured on a CHI 660B electrochemical workstation in a standard three-electrode system using the prepared samples as the working electrodes with an active area of ca. 0.5 cm$^2$. Platinum foil and a saturated calomel electrode (SCE) were used as the counter and reference electrodes, respectively. The visible light source ($\lambda > 420$ nm) was a 500 W Xe lamp with a 420 nm cutoff filter (JB450) to completely remove any radiation below 420 nm.

**2.4. Battery Performance Measurements.** The electrode slurries were prepared by mixing 80 wt % active material (reduced graphene oxide, pure $CuFe_2O_4$, $CuFe_2O_4$-G(0.1), and
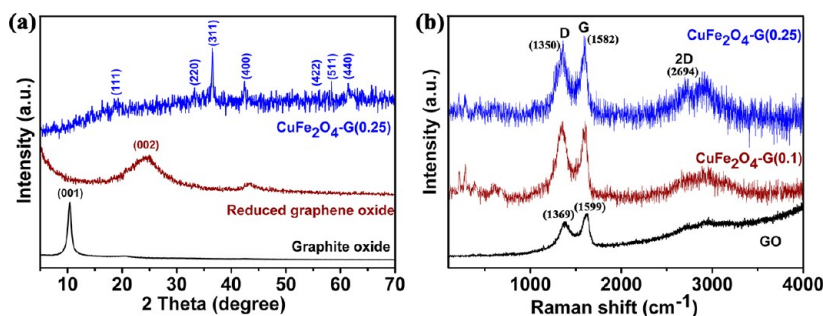
**Figure 1.** (a) XRD patterns of CuFe$_2$O$_4$-G(0.25), reduced graphene oxide, and graphite oxide in the range of 5−70°; (b) Raman spectra of CuFe$_2$O$_4$-G(0.25), CuFe$_2$O$_4$-G(0.1), and pure CuFe$_2$O$_4$.
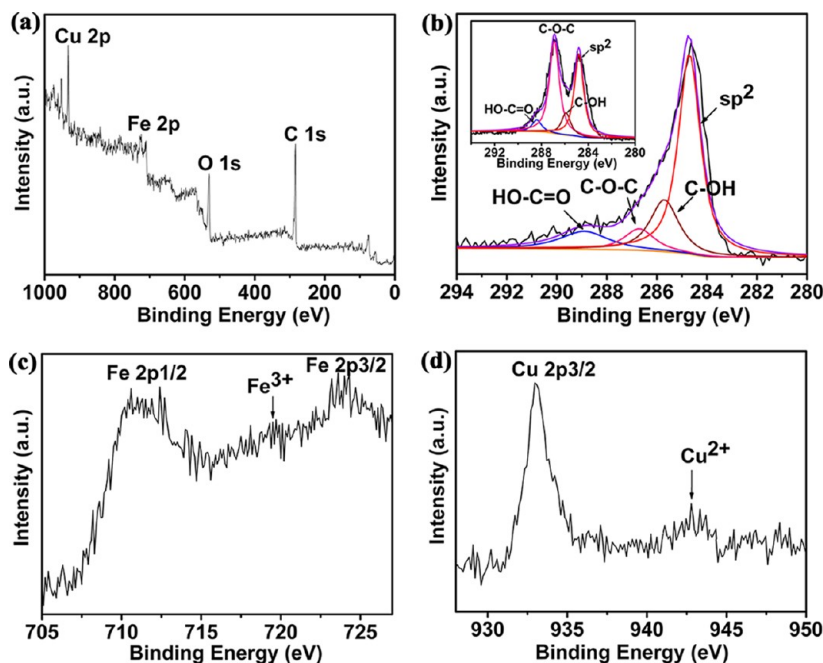


**Figure 2.** Wide (a) and deconvoluted (b−d) XPS spectra of the as-prepared CuFe$_2$O$_4$-G(0.25). The inset is C 1s XPS spectra of GO.

CuFe$_2$O$_4$-G(0.25), 10 wt % acetylene black (Super-P)) and 10 wt % polyvinylidene fluoride (PVDF) binder in N-methyl-2-pyrrolidinone (NMP). The slurries were coated on the Cu foils and dried at 120 °C for 2 h to remove the solvent. The dried electrodes were pressed and cut into small disks (10 mm in diameter). The small disks were further dried at 80 °C in a vacuum oven for 12 h before battery tests. Half cells using Li foil as both counter and reference electrodes were assembled with Lab-made Swagelok cells for the electrochemical measurements. LiPF6 (1 M) in ethylene carbonate and diethyl carbonate (EC/DEC, v/v = 1:1) solution was used as the electrolyte and a Celgard 2400 was used as the separator. Galvanostatic charge and discharge measurements were carried out in the voltage range between 0.01 and 3 V at different current densities using a LAND CT2001A electrochemical workstation at room temperature.

## 3. RESULTS AND DISCUSSION

**3.1. Structure and Morphology Characterization.** The XRD diffraction patterns of the as-prepared CuFe$_2$O$_4$-G(0.25) heteroarchitecture, reduced graphite oxide, and graphite oxide (GO) are shown in Figure 1a. For the CuFe$_2$O$_4$-G(0.25) heteroarchitecture, all the diffraction peaks can be indexed as cubic spinel CuFe$_2$O$_4$ while no typical diffraction peak of

graphite (002) or GO (001) is observable. It is speculated that the GO in the CuFe$_2$O$_4$-G heteroarchitecture was fully exfoliated due to the crystal growth of CuFe$_2$O$_4$ nanoparticles between the interlayer of GO sheets.[45−48]

Raman spectroscopy is one of the most important tools used for the characterization of carbon-based materials. For CuFe$_2$O$_4$-G(0.25) and CuFe$_2$O$_4$-G(0.1) shown in Figure 1b, both the G and D bands of Raman spectra shift to lower frequencies in comparison with that of GO, indicating that GO has been reduced to graphene.[51,52] Moreover, it is to be noted that the 2D band at 2694 cm$^{-1}$ can be also observed in the Raman spectrum of CuFe$_2$O$_4$-G(0.25), indicating the existence of monolayer graphene in the hybrid.[53−55] For CuFe$_2$O$_4$-G(0.25) and CuFe$_2$O$_4$-G(0.1), all the peaks in the 100−1000 cm$^{-1}$ region can be ascribed to the spinel CuFe$_2$O$_4$ phase.

The chemical composition and electronic structure of the CuFe$_2$O$_4$-G(0.25) nanocomposite was further investigated by X-ray photoelectron spectroscopy (XPS). The wide scan XPS spectrum and the narrow scan C 1s XPS spectrum of the CuFe$_2$O$_4$-G(0.25) nanocomposite are shown in Figure 2a,b, respectively. The inset of Figure 2b shows the C 1s XPS spectrum of the GO for comparison. The strong C 1s peak at 284.5 eV is related to graphitic carbon in graphene, while the other weaker ones are assigned to the oxygenated carbons,

indicating the deoxygenation process accompanying the reduction of graphene oxide as compared with much stronger peaks of those oxygenated carbons in GO (see inset of Figure 2b). Among the oxygen-containing groups on the carbon sheets, the epoxy groups were greatly reduced in the hybrid as compared with the starting GO. This result indicates that GO has been reduced to graphene with a tiny amount of residual oxygen-containing groups via hydrothermal reaction using ethanol as reducing agent.[38−40,56] The high-resolution XPS spectra of Cu 2p and Fe 2p (Figure 2c,d) show that Cu is in the 2+ and Fe is in the 3+ oxidation state in the nanocomposite, which is in good agreement with published work on $CuFe_2O_4$ particles.[57] These results further confirm the formation of $CuFe_2O_4$ in the nanocomposite.

The morphology and microstructure of the as-prepared pure $CuFe_2O_4$ and the $CuFe_2O_4$-G(0.25) nanocomposite were investigated by TEM and FESEM. As shown in Figure 3b,d
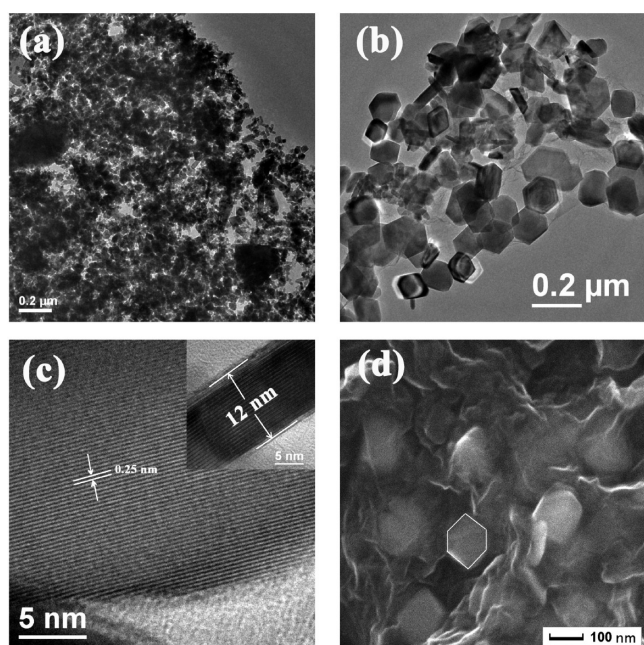


**Figure 3.** TEM image of (a) pure $CuFe_2O_4$; (b) $CuFe_2O_4$-G(0.25). (c) The high-resolution TEM image of $CuFe_2O_4$ nanoflake lying on a graphene sheet. The inset shows the thickness of the nanoflake is about 12 nm from the high-resolution TEM image. (d) The FESEM image of $CuFe_2O_4$-G(0.25).

and Figure 1S, Supporting Information, it can be clearly seen that the most of $CuFe_2O_4$ are hexagonal nanoflake and only a few of them are nanoparticle aggregates. Because of the different graphene content, there is a little change in the size and density of hexagonal $CuFe_2O_4$ nanoflakes on the graphene sheets. The average size of hexagonal $CuFe_2O_4$ nanoflakes is 170−200 nm for the low graphene content and 120−150 nm for the high graphene content, respectively. Figure 3c shows an HRTEM image of a $CuFe_2O_4$ nanoflake. The lattice fringes having an interlayer distance of 0.25 nm are ascribed to the (311) planes of $CuFe_2O_4$ with cubic spinel structure, which is consistent with the XRD results. The inset of Figure 3c shows an HRTEM image of the cross-sectional structure of $CuFe_2O_4$ nanoflake, and the thickness of the hexagonal nanoflake can be estimated to be approximately 12 nm. It should be noted that only the aggregates of $CuFe_2O_4$ nanoparticles (Figure 3a) can

be formed using the same synthesis conditions without adding GO.

Figure 4 shows the schematic illustration of a possible formation mechanism of the hexagonal $CuFe_2O_4$ nanoflakes in
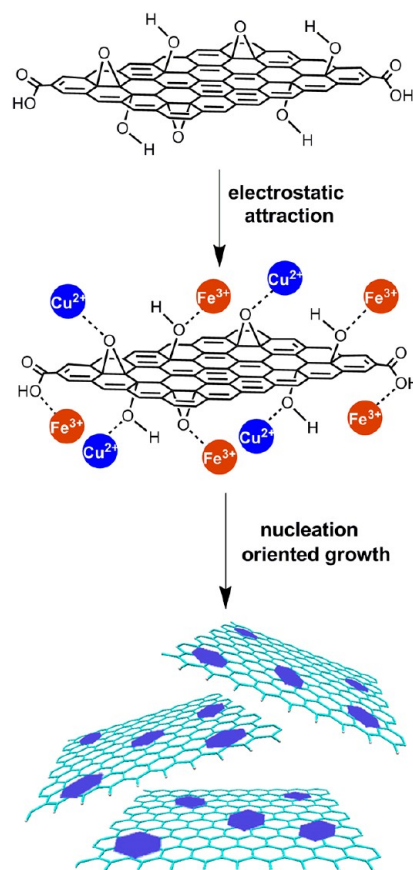


**Figure 4.** Schematic illustration of the formation mechanism of the hexagonal $CuFe_2O_4$ nanoflakes in the $CuFe_2O_4$-graphene hetero-architecture.

the $CuFe_2O_4$-graphene heteroarchitecture. It is well-known that GO consists of covalently attached oxygen-containing groups such as hydroxyl, epoxy, carbonyl, and carboxyl groups. Accordingly, the positively charged $Cu^{2+}$ and $Fe^{3+}$ ions can easily adsorb onto the negatively charged GO sheets via the electrostatic force. As illustrated in Figure 1Sc, Supporting Information, the $Cu^{2+}$ and $Fe^{3+}$ ions anchored on the carbon nanosheets in situ formed $CuFe_2O_4$ nanocrystals, and then, these tiny nanocrystals as nucleus grew into the hexagonal nanoflakes through oriented aggregation on the graphene template during the hydrothermal reaction. Evidence for oriented aggregation was also observed in our previous studies of graphene-$Cu_2O$ and graphene-$BiVO_4$ systems.[58,59]

Nitrogen isothermal adsorption−desorption measurements were performed to determine the Brunauer−Emmett−Teller (BET) surface area and the porosity of the pure $CuFe_2O_4$ and the $CuFe_2O_4$-G(0.25) heteroarchitecture. Figure 5 shows the nitrogen adsorption−desorption isotherms of the pure $CuFe_2O_4$ and the $CuFe_2O_4$-G(0.25) heteroarchitecture, respectively. Obviously, the isotherm of the $CuFe_2O_4$-G(0.25) heteroarchitecture exhibits a typical IUPAC type IV pattern, implying the existence of mesopores. The BET specific surface area of the $CuFe_2O_4$-G(0.25) heteroarchitecture is 204.28 $m^2 \cdot g^{-1}$, which is nearly 10 times as large as that of the pure
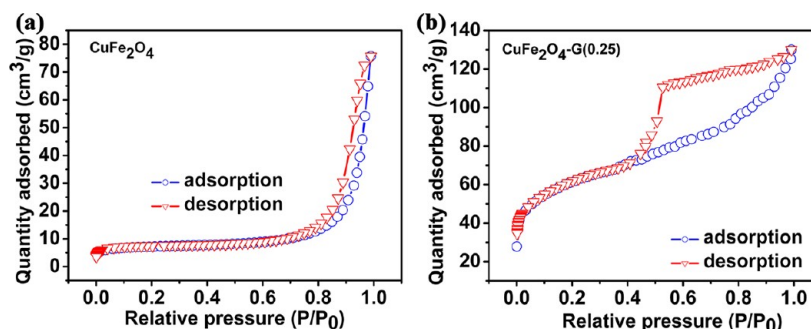
**Figure 5.** Nitrogen adsorption/desorption isotherm of (a) the pure $CuFe_2O_4$ and (b) the $CuFe_2O_4$-G(0.25) nanocomposite.



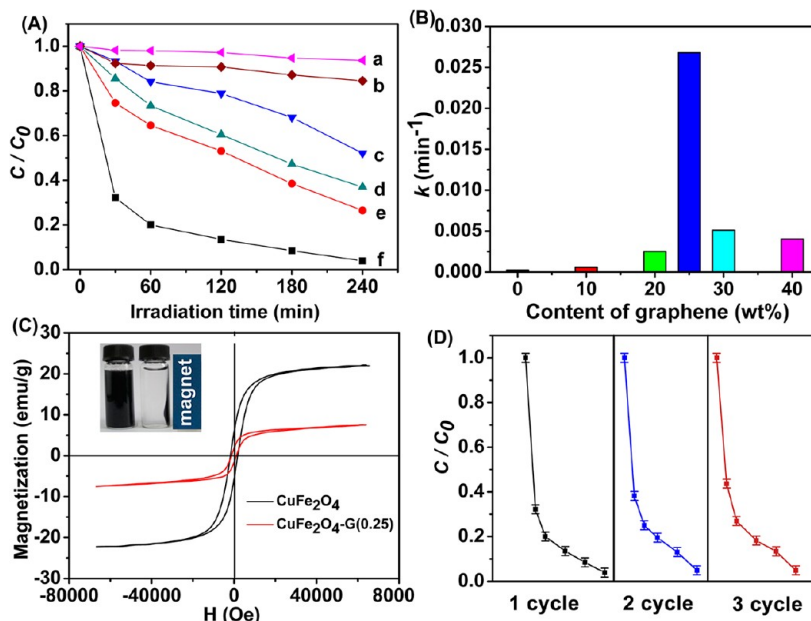**Figure 6.** (A) Photocatalytic degradation of MB over (a) pure $CuFe_2O_4$, (b) $CuFe_2O_4$-G(0.1), (c) $CuFe_2O_4$-G(0.2), (d) $CuFe_2O_4$-G(0.3), (e) $CuFe_2O_4$-G(0.4), and (f) $CuFe_2O_4$-G(0.25). (B) Rate constant for the photodecomposition of MB on $CuFe_2O_4$-graphene photocatalysts with differing graphene content. (C) Hysteresis loops of pure $CuFe_2O_4$ and $CuFe_2O_4$-G(0.25). The inset is the magnetic separation property of $CuFe_2O_4$-G(0.25) nanocomposite. (D) Photodegradation rate of MB in solution for three cycles using $CuFe_2O_4$-G(0.25) photocatalyst.

$CuFe_2O_4$ (22.82 m$^2$·g$^{-1}$). The large specific surface area of the nanocomposite can offer more adsorption and reaction sites as well as large electrode/electrolyte interface, consequently leading to enhanced photocatalytic activity and superior electrochemical performance for LIBs.

**3.2. Photocatalytic Properties and Mechanism.** The photocatalytic activities of the as-obtained $CuFe_2O_4$-graphene heteroarchitecture with differing graphene content were evaluated by the degradation of methylene blue (MB) under visible-light irradiation at 25 °C, and the results are shown in Figure 6A. The adsorption−desorption equilibrium solution of MB and $CuFe_2O_4$-G(0.25) was used as starting solution ($t = 0$ min). It can be seen that $CuFe_2O_4$ alone is almost photocatalytically inactive under visible light irradiation, whereas the introduction of graphene leads to a dramatic enhancement in the photocatalytic performance (Figure 6A). It is noted that the photocatalytic activity enhancement varied with the graphene content in the $CuFe_2O_4$-graphene heteroarchitecture; 25 wt % graphene in the $CuFe_2O_4$-graphene nanocomposite gave the best performance in photocatalytic activity (Figure 6A(f)).

It is well recognized that the photocatalytic degradation of MB follows a pseudofirst-order kinetics reaction. The rate equation for MB degradation can be written as follows:

$$k = -\frac{1}{t}\ln\frac{c}{c_0} \tag{1}$$

where $C_0$ and $C$ are the concentrations of MB when reaction time is 0 and $t$, respectively. Figure 6B shows the values for the pseudofirst-order rate constant ($k$) for the photodecomposition of MB by $CuFe_2O_4$-graphene photocatalysts with differing graphene content. It is obvious that $CuFe_2O_4$-G(0.25) gives the highest rate constant of 0.0267 min$^{-1}$ among these catalysts, and the photocatalytic activity of pure $CuFe_2O_4$ is negligible.

Magnetic properties of the as-obtained pure $CuFe_2O_4$ and the $CuFe_2O_4$-graphene nanocomposite with differing graphene content were measured by the VSM technique at 300 K, and the results are shown in Figure 6C and Figure 2S, Supporting Information. It can be clearly seen that all the samples show a typical hysteresis loop in the field range of ±80 kOe, indicating that all of them are soft magnetic semiconductor materials. The saturation magnetization (Ms), remanent magnetization (Mr), and coercivity (Hc) values are 22.21 emu/g, 6.70 emu/g, and
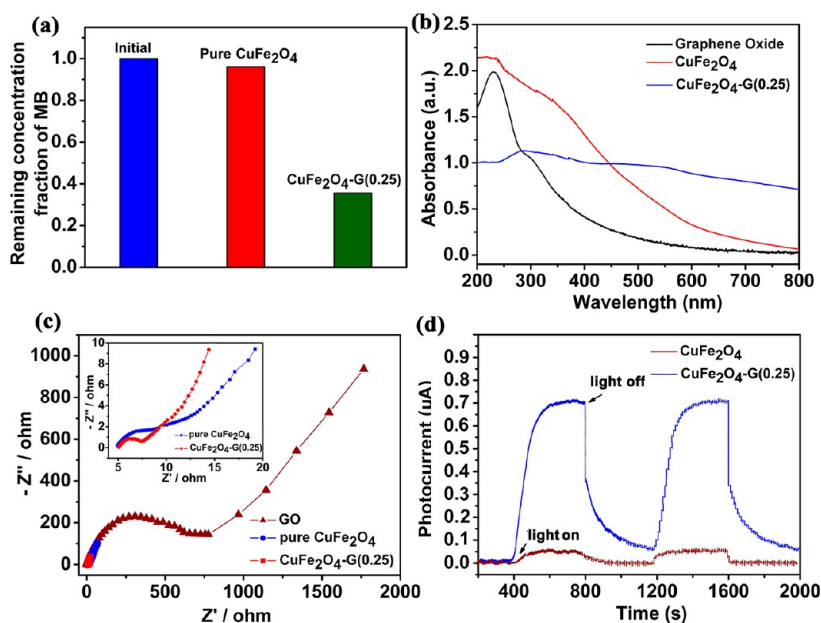
**Figure 7.** (a) Bar plot showing the remaining MB in solution after stirring in the dark for 60 min and reaching the adsorption−desorption equilibrium. (b) UV−vis absorbance spectra of graphene oxide, pure $CuFe_2O_4$, and $CuFe_2O_4$-G(0.25). (c) Electrochemical impedance spectra (EIS) of $CuFe_2O_4$-G(0.25), pure $CuFe_2O_4$, and GO. The inset is enlarged to show the impedance of $CuFe_2O_4$-G(0.25) and pure $CuFe_2O_4$. (d) Photocurrent transient responses of $CuFe_2O_4$-G(0.25) and pure $CuFe_2O_4$ electrodes under visible light irradiation, $[Na_2SO_4]$ = 0.5 M.

1704.41 Oe for the pure $CuFe_2O_4$, respectively, and 7.61 emu/g, 2.25 emu/g, and 1203.32 Oe for the $CuFe_2O_4$-G(0.25) nanocomposite, respectively. It should be pointed out that the saturation magnetization (Ms), remanent magnetization (Mr), and coercivity (Hc) values decreased with the increase of graphene content. The results suggest that the $CuFe_2O_4$-G(0.25) nanocomposite photocatalyst can be easily separated from the solution phase using an external magnet (see the inset of Figure 6C).

The $CuFe_2O_4$-graphene nanocomposite catalysts can be used repeatedly for the photocatalytic degradation of MB solution. Figure 6D shows the photocatalytic degradation of MB by the $CuFe_2O_4$-G(0.25) photocatalyst for three cycles under visible light irradiation. It can be seen that the photodegradation of MB still retained a rate of over 95% after three cycles, indicating that the magnetically separable photocatalyst $CuFe_2O_4$-G(0.25) is stable and effective for the degradation of organic pollutants in water. Moreover, there is no noticeable change in the structure and composition of $CuFe_2O_4$-G(25) photocatalyst after 3 cycles as analyzed using XRD, Raman, and XPS techniques.

As mentioned above, the $CuFe_2O_4$-G(0.25) nanocomposite shows the highest photocatalytic activity for MB degradation under visible light. The significant enhancement in photoactivity can be attributed to the remarkable synergistic effect of the combination of $CuFe_2O_4$ and the graphene sheets, leading to the enhanced adsorption of MB, the significant extension of the light absorption range, and the efficient separation of photogenerated carriers in the $CuFe_2O_4$ and graphene coupling system.

It is well believed that the preliminary adsorption of MB on the $CuFe_2O_4$-G(0.25) photocatalyst surface is a prerequisite for highly efficient photodegradation. As shown in Figure 7a, a large amount of MB molecules (ca. 60%) was adsorbed on the surface of $CuFe_2O_4$-G(0.25) after equilibrium, while the adsorption of MB on pure $CuFe_2O_4$ was unnoticeable. The

enhanced adsorptivity should be largely assigned to the π−π stacking and/or electrostatic attraction between MB and π-conjugation regions of the graphene sheets.[38]

Optical absorption properties of photocatalysts play an important role in the photocatalysis process, especially for the photodegradation contaminants under visible light irradiation. Figure 7b shows the UV−vis absorbance spectra of the graphene oxide, the pure $CuFe_2O_4$, and the $CuFe_2O_4$-G(0.25) nanocomposite. It is can be clearly seen that the graphene oxide exhibits an obvious characteristic absorption peak at about 230 nm, corresponding to π−π* transition of aromatic C=C bonds. For the $CuFe_2O_4$-G(0.25) nanocomposite, the typical absorption peak of graphene oxide at 230 nm disappears and the absorption covers the whole visible region due to the introduction of graphene, indicating the $CuFe_2O_4$-G(0.25) heteroarchitecture can be used as photocatalyst in practical environmental remediation under visible light irradiation.

To analyze the synergistic effect between $CuFe_2O_4$ and graphene, the electrochemical impedance technique was employed to characterize electrical conductivity and the results are shown in Figure 7c. It can be seen that the impedance plot of the $CuFe_2O_4$-G(0.25) nanocomposite has the smallest radius among the three electrodes, implying the lowest resistance of the interfacial charge transfer. A significant decrease in charge-transfer resistance of the $CuFe_2O_4$-G(0.25) nanocomposite can be largely attributed to the reduction of graphene oxide in the hydrothermal reaction process. A smaller charge-transfer resistance is favorable for the enhancement of photocatalytic activity, since the photogenerated electrons from the $CuFe_2O_4$ nanoflakes can transfer easily from the conduction band to the reduced graphene oxide which has superior electrical conductivity, effectively preventing a direct recombination of electrons and holes.

The synergistic effect between $CuFe_2O_4$ and graphene can be further examined by the transient photocurrent responses technique which is a reliable way to confirm the efficient
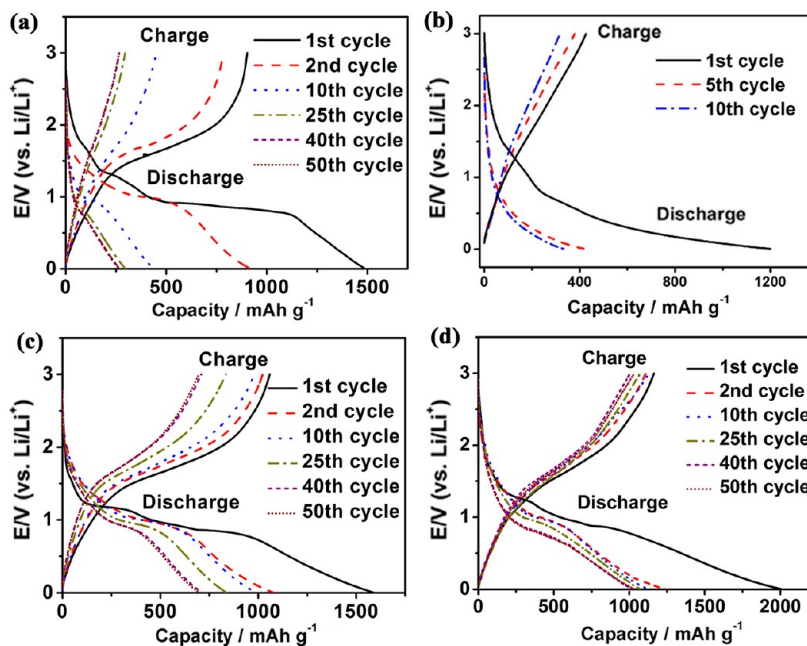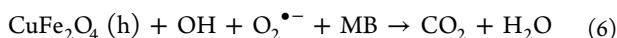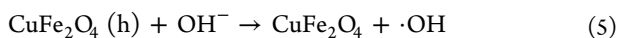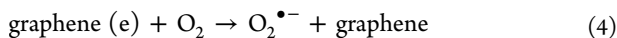
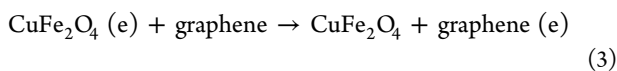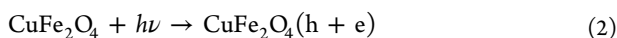**Figure 8.** Charge/discharge curves of (a) pure $CuFe_2O_4$, (b) reduced graphene oxide, (c) $CuFe_2O_4$-G(0.1), and (d) $CuFe_2O_4$-G(0.25) between 0.01 and 3 V at a current density of 100 mA g$^{-1}$.

separation of photogenerated carriers in the $CuFe_2O_4$ and graphene coupling system. As shown in Figure 7d, the photocurrent measurements were carried out for the pure $CuFe_2O_4$ and the $CuFe_2O_4$-G(0.25) nanocomposite after deposition on ITO electrodes via several on−off cycles of the visible-light irradiation. The photocurrent of the $CuFe_2O_4$-G(0.25) nanocomposite electrode (0.71 $\mu$A) is about 15 times as high as that of the pure $CuFe_2O_4$ electrode (0.05 $\mu$A), indicating a greatly enhanced separation efficiency of photo-induced electrons and holes because of the introduction of graphene. Figure 3S, Supporting Information, shows the transient photocurrent responses of $CuFe_2O_4$-graphene nano-composites with differing graphene content, it can be clearly seen that $CuFe_2O_4$-G(0.25) nanocomposite electrode gives the highest photocurrent value among the all samples, indicating that there is the most synergistic effect between $CuFe_2O_4$ and the graphene sheets. This can explain why $CuFe_2O_4$-G(0.25) nanocomposite has the best photocatalytic activity.

On the basis of the above discussion, a possible mechanism for photocatalytic activity enhancement can be suggested as follows:

$$CuFe_2O_4 + h\nu \rightarrow CuFe_2O_4(h + e) \qquad (2)$$

$$CuFe_2O_4 (e) + graphene \rightarrow CuFe_2O_4 + graphene (e) \qquad (3)$$

$$graphene (e) + O_2 \rightarrow O_2^{\bullet-} + graphene \qquad (4)$$

$$CuFe_2O_4 (h) + OH^- \rightarrow CuFe_2O_4 + \cdot OH \qquad (5)$$

$$CuFe_2O_4 (h) + OH + O_2^{\bullet-} + MB \rightarrow CO_2 + H_2O \qquad (6)$$

Upon irradiation with visible light, electrons (e) and holes (h) are generated on the $CuFe_2O_4$ surface (Reaction 2), followed by instant transfer of photogenerated electrons to graphene sheets which are known as efficient electron acceptors via a percolation mechanism (Reaction 3). Then, the negatively charged graphene sheets can activate the dissolved oxygen to produce superoxide anion radicals (Reaction 4), while the holes are scavenged by the adsorbed water to form hydroxyl radicals (Reaction 5). Finally, these active species (holes, superoxide anion radicals, and hydroxyl radicals) oxidize the MB molecules adsorbed on the active sites of the $CuFe_2O_4$-graphene heteroarchitecture through the $\pi-\pi$ stacking and/or electro-static attraction (Reaction 6).

**3.3. Electrochemical Properties.** As will be seen, the $CuFe_2O_4$-graphene heteroarchitecture can also be used for energy storage as anode material with excellent electrochemical properties in lithium-ion batteries. Figure 8 shows the charge/discharge curves of the pure $CuFe_2O_4$, the reduced graphene oxide, the $CuFe_2O_4$-G(0.1) nanocomposite, and the $CuFe_2O_4$-G(0.25) nanocomposite electrodes at different cycles between 0.01 and 3 V at a current density of 100 mA g$^{-1}$. As shown in Figure 8a, the first discharge and charge curves for the pure $CuFe_2O_4$ electrode exhibit voltage plateaus at around 1.0 and 1.5 V, respectively, corresponding to reduction/oxidation reactions during lithium insertion/extraction. The electro-chemical reversible reaction can be expressed as

$$CuFe_2O_4 + 8e^- + 8Li^+ \Leftrightarrow Cu^0 + 2Fe^0 + 4Li_2O \qquad (7)$$
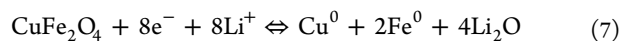
Assuming that 8 Li$^+$ ions are reversibly inserted and extracted, a specific reversible capacity of 895 mAh g$^{-1}$ can be obtained. The first discharge and charge capacities of the pure $CuFe_2O_4$ electrode are 1450 and 875 mAh g$^{-1}$, respectively, with a Coulombic efficiency of 60.3%. The irreversible capacity loss of the $CuFe_2O_4$ electrode for the first cycle is probably due to incomplete conversion reaction and the solid electrolyte interface (SEI) layer formation at the electrode/electrolyte interface caused by the reduction of electrolyte.

Figure 8b shows the charge/discharge curves of the pure graphene electrode for the first three cycles. No voltage plateaus can be observed from both charge and discharge curves of the pure graphene electrode. The reversible capacity of the reduced graphene oxide electrode for the first cycle is
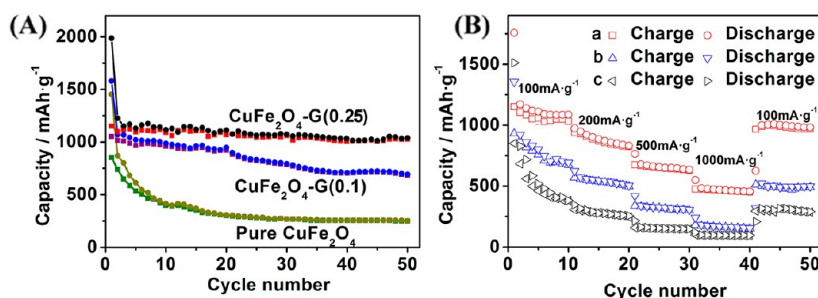
**Figure 9.** (A) Comparison of cycle performance of pure $CuFe_2O_4$, $CuFe_2O_4$-G(0.1), and $CuFe_2O_4$-G(0.25). (B) Comparison of rate performance of (a) $CuFe_2O_4$-G(0.25), (b) $CuFe_2O_4$-G(10), and (c) pure $CuFe_2O_4$.

426 mAh $g^{-1}$ with a Coulombic efficiency of 33%. The relatively large first cycle irreversible capacity of the reduced graphene oxide electrode is due to SEI layer formation and spontaneous stacking of graphene nanosheets during the first lithiation. When graphene is combined with $CuFe_2O_4$ to form the nanocomposite, the reversible capacity of the electrode can be significantly improved. As shown in Figure 8c, the first cycle discharge and charge capacities for the $CuFe_2O_4$-G(0.1) nanocompsoite electrode are 1605 and 1062 mAh $g^{-1}$, with a Coulombic efficiency of 66%. When the graphene content reaches 25 wt % in the nanocomposite, the first cycle discharge and charge capacities are 2000 and 1165 mAh $g^{-1}$, with a Coulombic efficiency of 58% (Figure 8d). The first cycle discharge and charge curves for both the $CuFe_2O_4$-G(0.1) and $CuFe_2O_4$-G(0.25) nanocomposite electrodes exhibit similar voltage plateaus as observed from the pure $CuFe_2O_4$ electrode, indicating similar redox reactions occur during the charge/discharge processes.[33−35] When comparing the first cycle discharge curves for the above four electrodes, it is found that, when more graphene is added to $CuFe_2O_4$, shorter voltage plateau at about 1.0 V but larger specific capacities are obtained. It is speculated that graphene could contribute more Li insertion/extraction sites than $CuFe_2O_4$ in the nanocomposite, especially in the case of higher graphene content. Although the pure graphene electrode in the present study only delivers a discharge capacity of about 1200 mAh $g^{-1}$, the discharge capacity can be greatly improved when the graphene nanosheets are largely exfoliated, which is exactly the case with the $CuFe_2O_4$-graphene nanocomposite. As reported by Lian and Wang et al., the exfoliated graphene nanosheets with a curled morphology can deliver a discharge capacity of about 2035 mAh $g^{-1}$ and a charge capacity of about 1264 mAh $g^{-1}$ for the first cycle.[60] This could probably explain why the first cycle reversible capacity of the $CuFe_2O_4$-G(0.25) nanocomposite electrode is much larger than that of the pure $CuFe_2O_4$ or the theoretical capacity of $CuFe_2O_4$. However, the increased graphene content in the nanocomposite could probably result in a larger irreversible capacity loss for the first cycle due to deteriorated SEI layer formation induced by the increased surface area.

Figure 9A shows the cycle performance of the pure $CuFe_2O_4$ electrode, the $CuFe_2O_4$-G(0.1) electrode, and the $CuFe_2O_4$-G(0.25) electrode at a current density of 100 mA $g^{-1}$ for 50 cycles. It is clear that the $CuFe_2O_4$-G(0.25) electrode exhibits much larger reversible capacity and better cycle performance than the pure $CuFe_2O_4$ electrode and the $CuFe_2O_4$-G(0.1) electrode. After 50 cycles, the pure $CuFe_2O_4$ electrode can deliver a reversible capacity of about 225 mAh $g^{-1}$, which is only 26% of the reversible capacity for the first cycle. The

introduction of graphene to $CuFe_2O_4$ can greatly improve the cycle performance of the electrode. In sharp contrast, after 50 cycles, the reversible capacity of the $CuFe_2O_4$-G(0.1) electrode decreases from 1062 to 687 mAh $g^{-1}$ while the reversible capacity of the $CuFe_2O_4$-G(0.25) electrode decreases from 1165 to 1031 mAh $g^{-1}$. Besides cycle performance, rate capability is also very important for lithium-ion batteries, especially for high power applications. Figure 9B compares the rate capability of the pure $CuFe_2O_4$ electrode, the $CuFe_2O_4$-G(0.1) electrode and the $CuFe_2O_4$-G(0.25) electrode. It can be seen that the $CuFe_2O_4$-G(0.25) electrode exhibits the best rate capability among the three electrodes. In particular, the reversible capacity of the $CuFe_2O_4$-G(0.25) still retains 500 mAh $g^{-1}$ even at a high current density of 1000 mA $g^{-1}$, which is much higher than that of the pure $CuFe_2O_4$ electrode or the $CuFe_2O_4$-G(0.1) electrodes. Moreover, when the current density returns to 100 mA $g^{-1}$ after 40 cycles, the reversible capacity of the $CuFe_2O_4$-G(0.25) electrode nearly recovers its initial value, indicating good stability for the nanocomposite.

The superior cycle performance and rate capability of the $CuFe_2O_4$-graphene electrode can be attributed to its unique heteroarchitechture, leading to the remarkable synergistic effect between $CuFe_2O_4$ nanoflakes and the graphene nanosheets. For the $CuFe_2O_4$-G(0.25) heteroarchitecture, the $CuFe_2O_4$ nanoflakes are well-dispersed and anchored on the graphene sheets, and the interaction between the nanoflakes and the graphene sheets not only suppresses the aggregation of $CuFe_2O_4$ nanoparticles but also prevents the restacking of graphene nanosheets, resulting in a large electrode/electrolyte interface area. The enhanced interface area of the nanocomposite not only provides more lithium insertion/extraction sites but also facilitates fast charge transfer between the active material and the electrolyte. In the case of pure $CuFe_2O_4$, the nanoparticles may aggregate into several hundred nanometer clusters with reduced interface area, which block the penetration of electrolyte, resulting in reduced interface area. These clusters could be pulverized due to the high strain induced by huge volume change during the charge/discharge processes, which may cause the loss of electrical contact between the $CuFe_2O_4$ nanoparticles and the current collector, thus leading to severe capacity loss during the cycling as can be seen from Figure 9A. The unique heteroarchitechture of $CuFe_2O_4$-graphene possesses good stability during the charge/discharge process due to the flexible two-dimensional network structure of graphene sheets, which could provide an elastic buffer space to accommodate the volume expansion/contraction of $CuFe_2O_4$ nanoflakes along the direction of the hexagonal planes, thus resulting in excellent cycling stability. Moreover, the good rate capability of the $CuFe_2O_4$-graphene

11707

dx.doi.org/10.1021/ie301347j | Ind. Eng. Chem. Res. 2012, 51, 11700−11709

heteroarchitecture comes from the significantly improved electrical conductivity of the electrode due to the conductive network constructed by the graphene sheets, which makes the $CuFe_2O_4$ nanoflakes electrochemically active since charge carriers can be effectively and rapidly conducted back and forth from the $CuFe_2O_4$ nanoflakes to the current collector.

## 4. CONCLUSION

In summary, a multifunctional $CuFe_2O_4$-graphene heteroarchitecture with differing graphene content has been successfully prepared via a one-step hydrothermal method without the use of any surfactants. TEM observations indicate that graphene sheets are exfoliated and decorated with hexagonal $CuFe_2O_4$ nanoflakes, due to the fact that the graphene sheets play the role of template to allow two-dimensional planar growth. The photocatalytic activity measurements demonstrate that the combination of $CuFe_2O_4$ with graphene sheets results in a dramatic conversion of the inert $CuFe_2O_4$ into a highly active catalyst for the degradation of methylene blue (MB) under visible light irradiation. Moreover, the $CuFe_2O_4$-graphene (with 25 wt % graphene) heteroarchitecture as the anode material for lithium-ion batteries shows a high specific reversible capacity up to 1165 mAh g$^{-1}$ with good cycling stability and rate capability. The superior photocatalytic activity and electrochemical performance of the $CuFe_2O_4$-graphene can be attributed to its unique heteroarchitechture, which provides the remarkable synergistic effect between the $CuFe_2O_4$ and the graphene sheets.

## ■ ASSOCIATED CONTENT

### Ⓢ Supporting Information

Typical TEM images, hysteresis loops, and photocurrent transient responses of $CuFe_2O_4$-graphene nanocomposite with different graphene content. This material is available free of charge via the Internet at http://pubs.acs.org.

## ■ AUTHOR INFORMATION

### Corresponding Author
*Tel.: +86-25-84305667 (X.W.). Fax: +86-25-8431-5054 (X.W.). E-mail: wxin@public1.ptt.js.cn (X.W.); xqsun@cczu.edu.cn (X.Q.S.); jasonxiahui@gmail.com (H.X.).

### Notes
The authors declare no competing financial interest.

## ■ ACKNOWLEDGMENTS

## ■ REFERENCES

(1) Hoffmann, M. R.; Martin, S. T.; Choi, W.; Bahnemann, D. W. Environmental applications of semiconductor photocatalysis. *Chem. Rev.* **1995**, *95*, 69−96.

(2) Kumaresan, L.; Mahalakshmi, M.; Palanichamy, M.; Murugesan, V. Synthesis, characterization, and photocatalytic activity of Sr$^{2+}$ doped TiO$_2$ nanoplates. *Ind. Eng. Chem. Res.* **2010**, *49*, 1480−1485.

(3) Ravelli, D.; Dondi, D.; Fagnoni, M.; Albini, A. Photocatalysis: A multi-faceted concept for green chemistry. *Chem. Soc. Rev.* **2009**, *38*, 1999−2011.

(4) Smith, Y. R.; Kar, A.; Subramanian, V. R. Investigation of physicochemical parameters that influence photocatalytic degradation of methyl orange over TiO$_2$ nanotubes. *Ind. Eng. Chem. Res.* **2009**, *48*, 10268−10276.

(5) Li, L.; Chu, Y.; Liu, Y.; Dong, L. Template-free synthesis and photocatalytic properties of novel Fe$_2$O$_3$ hollow spheres. *J. Phys. Chem. C* **2007**, *111*, 2123−2127.

(6) Shu, X.; He, J.; Chen, D. Visible-light-induced photocatalyst based on nickel titanate nanoparticles. *Ind. Eng. Chem. Res.* **2008**, *47*, 4750−4753.

(7) Guo, R. Q.; Fang, L. A.; Dong, W.; Zheng, F. G.; Shen, M. R. Enhanced photocatalytic activity and ferromagnetism in Gd doped BiFeO$_3$ nanoparticles. *J. Phys. Chem. C* **2010**, *114*, 21390−21396.

(8) Cai, L.; Liao, X.; Shi, B. Using collagen fiber as a template to synthesize TiO$_2$ and Fex/TiO$_2$ nanofibers and their catalytic behaviors on the visible light-assisted degradation of orange II. *Ind. Eng. Chem. Res.* **2010**, *49*, 3194−3199.

(9) Liang, Y. Y.; Wang, H. L.; Casalongue, H. S.; Chen, Z.; Dai, H. J. TiO$_2$ nanocrystals grown on graphene as advanced photocatalytic hybrid materials. *Nano Res.* **2010**, *3*, 701−705.

(10) Zhang, A.; Zhang, J. Effects of europium doping on the photocatalytic behavior of BiVO$_4$. *J. Hazard. Mater.* **2010**, *173*, 265−272.

(11) Vijayan, B. K.; Dimitrijevic, N. M.; Wu, J. S.; Gray, K. A. The effects of Pt doping on the structure and visible light photoactivity of titania nanotubes. *J. Phys. Chem. C* **2010**, *114*, 21262−21269.

(12) Cai, W. D.; Chen, F.; Shen, X. X.; Chen, L. J.; Zhang, J. L. Enhanced catalytic degradation of AO7 in the CeO$_2$-H$_2$O$_2$ system with Fe$^{3+}$ doping. *Appl. Catal., B* **2010**, *101*, 160−168.

(13) Shylesh, S.; Schunemann, V.; Thiel, W. R. Magnetically separable nanocatalysts: Bridges between homogeneous and heterogeneous catalysis. *Angew. Chem., Int. Ed.* **2010**, *49*, 3428−3459.

(14) Faungnawakij, K.; Kikuchi, R.; Shimoda, N.; Fukunaga, T.; Eguchi, K. Effect of thermal treatment on activity and durability of CuFe$_2$O$_4$−Al$_2$O$_3$ composite catalysts for steam reforming of dimethyl ether. *Angew. Chem., Int. Ed.* **2008**, *47*, 9314−9317.

(15) Shin, H.; Choi, S. Mechanism of M Ferrites (M=Cu and Ni) in the CO$_2$ decomposition reaction. *Chem. Mater.* **2001**, *13*, 1238−1242.

(16) Faungnawakij, K.; Shimoda, N.; Fukunaga, T.; Kikuchi, R.; Eguchi, K. Crystal structure and surface species of CuFe$_2$O$_4$ spinel catalysts in steam reforming of dimethyl ether. *Appl. Catal., B* **2009**, *92*, 341−350.

(17) Guo, X.; Lu, X.; Fang, X.; Mao, Y.; Wang, Z.; Chen, L.; Xu, X.; Yang, H.; Liu, Y. Lithium storage in hollow spherical ZnFe$_2$O$_4$ as anode materials for lithium ion batteries. *Electrochem. Commun.* **2010**, *12*, 847−850.

(18) Li, Z. H.; Zhao, T. P.; Zhan, X. Y.; Gao, D. S.; Xiao, Q. Z.; Lei, G. T. High capacity three-dimensional ordered macroporous CoFe$_2$O$_4$ as anode material for lithium ion batteries. *Electrochim. Acta* **2010**, *55*, 4594−4598.

(19) Zhao, Y.; Li, J.; Ding, Y.; Guan, L. Enhancing the lithium storage performance of iron oxide composites through partial substitution with Ni$^{2+}$ or Co$^{2+}$. *J. Mater. Chem.* **2011**, *21*, 19101−19105.

(20) Jin, L.; Qiu, Y.; Deng, H.; Li, W.; Li, H.; Yang, S. Hollow CuFe$_2$O$_4$ spheres encapsulated in carbon shells as an anode material for rechargeable lithium-ion batteries. *Electrochim. Acta* **2011**, *56*, 9127−9132.

(21) Bomio, M.; Lavela, P.; Tirado, J. L. $^{57}$Fe Mussbauer spectroscopy and electron microscopy study of metal extraction from CuFe$_2$O$_4$ electrodes in lithium cells. *ChemPhysChem* **2007**, *8*, 1999−2007.

(22) Nu, Y.; Qin, Q. Nanocrystalline transition metal ferrite thin films prepared by an electrochemical route for Li-ion batteries. *J. Power Sources* **2005**, *142*, 292−297.

(23) Lee, W. H.; Park, J.; Sim, S. H.; Jo, S. B.; Kim, K. S.; Hong, B. H.; Cho, K. Transparent flexible organic transistors based on monolayer graphene electrodes on plastic. *Adv. Mater.* **2011**, *23*, 1752−1756.

(24) Chen, S.; Zhu, J.; Wang, X. From graphene to metal oxide nanolamellas: A phenomenon of morphology transmission. *ACS Nano* **2010**, *4*, 6212−6218.

(25) Zhu, S. E.; Shabani, R.; Rho, J.; Kim, Y.; Hong, B. H.; Ahn, J.-H.; Cho, H. J. Graphene-based bimorph microactuators. *Nano Lett.* **2011**, *11*, 977−981.

(26) Wang, D. R.; Ye, G.; Wang, X. L.; Wang, X. G. Graphene functionalized with azo polymer brushes: surface-initiated polymerization and photoresponsive properties. *Adv. Mater.* **2011**, *23*, 1122−1125.

(27) Cao, A. N.; Liu, Z.; Chu, S. S.; Wu, M. H.; Ye, Z. M.; Cai, Z. W.; Chang, Y. L.; Wang, S. F.; Gong, Q. H.; Liu, Y. F. A facile one-step method to produce graphene-CdS quantum dot nanocomposites as promising otoelectronic materials. *Adv. Mater.* **2010**, *22*, 103−106.

(28) Zhan, Y. Q.; Yang, X. L.; Guo, H.; Yang, J.; Meng, F. B.; Liu, X. B. Cross-linkable nitrile functionalized graphene oxide/poly(arylene ether nitrile) nanocomposite films with high mechanical strength and thermal stability. *J. Mater. Chem.* **2012**, *22*, 5602−5608.

(29) Liu, Z. F.; Liu, Q.; Huang, Y.; Ma, Y. F.; Yin, S. G.; Zhang, X. Y. Organic photovoltaic devices based on a novel acceptor material: Graphene. *Adv. Mater.* **2008**, *20*, 3924−3930.

(30) Xu, C.; Wang, X.; Zhu, J. W.; Yang, X. J.; Lu, L. Deposition of Co₃O₄ nanoparticles onto exfoliated graphite oxide sheets. *J. Mater. Chem.* **2008**, *18*, 5625−5629.

(31) Zhu, J. W.; Zeng, G. Y.; Nie, F. D.; Xu, X. M.; Chen, S.; Han, Q. F.; Wang, X. Decorating graphene oxide with CuO nanoparticles in a water-isopropanol system. *Nanoscale* **2010**, *2*, 988−994.

(32) Li, Y. M.; Lv, X. J.; Lu, J.; Li, J. H. Preparation of SnO₂-nanocrystal/graphene-nanosheets composites and their lithium storage ability. *J. Phys. Chem. C* **2010**, *114*, 21770−21774.

(33) Wu, Z. S.; Ren, W.; Wen, L.; Gao, L.; Zhao, J.; Chen, Z.; Zhou, G.; Li, F.; Cheng, H. M. Graphene anchored with Co₃O₄ nanoparticles as anode of lithium ion batteries with enhanced reversible capacity and cyclic performance. *ACS Nano* **2010**, *4*, 3187−3194.

(34) Zhu, X.; Zhu, Y.; Murali, S.; Stoller, M. D.; Ruoff, R. S. Nanostructured reduced graphene oxide/Fe₂O₃ composite as a high-performance anode material for lithium ion batteries. *ACS Nano* **2011**, *5*, 3333−3338.

(35) Zhou, G.; Wang, D. W.; Li, F.; Zhang, L.; Li, N.; Wu, Z. S.; Wen, L.; Lu, G. Q.; Cheng, H. M. Graphene-wrapped Fe₃O₄ anode material with improved reversible capacity and cyclic stability for lithium ion batteries. *Chem. Mater.* **2010**, *22*, 5306−5313.

(36) Fu, Y. S.; Wan, Y. H.; Xia, H.; Wang, X. Nickel ferrite-graphene heteroarchitectures: Toward high-performance anode materials for lithium-ion batteries. *J. Power Sources* **2012**, *213*, 338−342.

(37) Li, Y. M.; Lv, X. J.; Lu, J.; Li, J. H. Preparation of SnO₂-nanocrystal/graphene-nanosheets composites and their lithium storage ability. *J. Phys. Chem. C* **2010**, *114*, 21770−21774.

(38) Zhang, H.; Lv, X.; Li, Y.; Wang, Y.; Li, J. P25-graphene composite as a high performance photocatalyst. *ACS Nano* **2010**, *4*, 380−386.

(39) Akhavan, O. Graphene nanomesh by ZnO nanorod photocatalysts. *ACS Nano* **2010**, *4*, 4174−4180.

(40) Zhang, Y.; Tang, Z. R.; Fu, X.; Xu, Y. J. TiO₂-graphene nanocomposites for gas-phase photocatalytic degradation of volatile aromatic pollutant: Is TiO₂-graphene truly different from other TiO₂-carbon composite materials? *ACS Nano* **2010**, *4*, 7303−7314.

(41) Yoo, D. H.; Tran, V. C.; Pham, V. H.; Chung, J. S.; Khoa, N. T.; Kim, E. J.; Hahn, S. H. Enhanced photocatalytic activity of graphene oxide decorated on TiO₂ films under UV and visible irradiation. *Curr. Appl. Phys.* **2011**, *11*, 805−808.

(42) Akhavan, O. Photocatalytic reduction of graphene oxides hybridized by ZnO nanoparticles in ethanol. *Carbon* **2011**, *49*, 11−18.

(43) Xu, T. G.; Zhang, L. W.; Cheng, H. Y.; Zhu, Y. F. Significantly enhanced photocatalytic performance of ZnO via graphene hybridization and the mechanism study. *Appl. Catal., B* **2011**, *101*, 382−387.

(44) Chen, C.; Cai, W.; Long, M.; Zhou, B.; Wu, Y.; Wu, D.; Feng, Y. Synthesis of visible-light responsive graphene oxide/TiO₂ composites with p/n heterojunction. *ACS Nano* **2010**, *4*, 6425−6432.

(45) Fu, Y. S.; Wang, X. Magnetically separable ZnFe₂O₄-graphene catalyst and its high photocatalytic performance under visible light irradiation. *Ind. Eng. Chem. Res.* **2011**, *50*, 7210−7217.

(46) Fu, Y. S.; Chen, H. Q.; Sun, X. Q.; Wang, X. Combination of cobalt ferrite and graphene: High-performance and recyclable visible-light photocatalysis. *Appl. Catal., B* **2012**, *111−112*, 280−287.

(47) Fu, Y. S.; Chen, H. Q.; Sun, X. Q.; Wang, X. Graphene-supported nickel ferrite: A magnetically separable photocatalyst with high activity under visible light. *AIChE J.* **2011**, DOI: 10.1002/aic.13716.

(48) Fu, Y. S.; Xiong, P.; Chen, H. Q.; Sun, X. Q.; Wang, X. High photocatalytic activity of magnetically separable manganese ferrite-graphene heteroarchitectures. *Ind. Eng. Chem. Res.* **2012**, *51*, 725−731.

(49) Hummers, W. S.; Offeman, R. E. Preparation of graphitic oxide. *J. Am. Chem. Soc.* **1958**, *80*, 1339−1339.

(50) Wang, H.; Hao, Q.; Yang, X.; Lu, L.; Wang, X. Effect of graphene oxide on the properties of its composite with polyaniline. *ACS Appl. Mater. Interfaces* **2010**, *2*, 821−828.

(51) Stankovich, S.; Dikin, D. A.; Piner, R. D.; Kohlhaas, K. A.; Kleinhammes, A.; Jia, Y.; Wu, Y.; Nguyen, S. T.; Ruoff, R. S. Synthesis of graphene-based nanosheets via chemical reduction of exfoliated graphite oxide. *Carbon* **2007**, *45*, 1558−1565.

(52) Lambert, T. N.; Chavez, C. A.; Hernandez-Sanchez, B.; Lu, P.; Bell, N. S.; Ambrosini, A.; Friedman, T.; Boyle, T. J.; Wheeler, D. R.; Huber, D. L. Synthesis and characterization of titania-graphene nanocomposites. *J. Phys. Chem. C* **2009**, *113*, 19812−19823.

(53) Vasu, K. S.; Chakraborty, B.; Sampath, S.; Sood, A. K. Probing top-gated field effect transistor of reduced graphene oxide monolayer made by dielectrophoresis. *Solid State Commun.* **2010**, *150*, 1295−1298.

(54) Ray, S. C.; Saha, A.; Basiruddin, S. K.; Roy, S. S.; Jana, N. R. Polyacrylate-coated graphene-oxide and graphene solution via chemical route for various biological application. *Diamond Relat. Mater.* **2011**, *20*, 449−453.

(55) Ferrari, A. C.; Meyer, J. C.; Scardaci, V.; Casiraghi, C.; Lazzeri, M.; Mauri, F.; Piscanec, S.; Jiang, D.; Novoselov, K. S.; Roth, S.; Geim, A. K. Raman spectrum of graphene and graphene layers. *Phys. Rev. Lett.* **2006**, *97*, 187401.

(56) Nethravathi, C.; Rajamathi, M. Chemically modified graphene sheets produced by the solvothermal reduction of colloidal dispersions of graphite oxide. *Carbon* **2008**, *46*, 1994−1998.

(57) Nedkov, I.; Vandenberghe, R. E.; Marinova, T.; Thailhades, Ph.; Merodiiska, T.; Avramova, I. Magnetic structure and collective Jahn−Teller distortions in nanostructured particles of CuFe₂O₄. *Appl. Surf. Sci.* **2006**, *253*, 2589−2596.

(58) Xu, C.; Wang, X.; Yang, L.; Wu, Y. Fabrication of a graphene-cuprous oxide composite. *J. Solid State Chem.* **2009**, *182*, 2486−2490.

(59) Fu, Y.; Sun, X.; Wang, X. BiVO₄-graphene catalyst and its high photocatalytic performance under visible light irradiation. *Mater. Chem. Phys.* **2011**, *131*, 325−330.

(60) Lian, P.; Zhu, X.; Liang, S.; Li, Z.; Yang, W.; Wang, H. Large reversible capacity of high quality graphene sheets as an anode material for lithium-ion batteries. *Electrochim. Acta* **2009**, *55*, 3909−3914.